Piece-By-Piece Shape-Morphing: Engineering Compatible Auxetic and Non-Auxetic Lattices to Improve Soft Robot Performance in Confined Spaces

Yusuf Dikici, Hao Jiang, Bo Li, Kathryn A. Daltorio, and Ozan Akkus*

Shape-morphing capabilities of metamaterials can be expanded by developing approaches that enable the integration of different types of cellular structures. Herein, a rational material design process is presented that fits together auxetic (anti-tetrachiral) and non-auxetic (the novel nodal honeycomb) lattice structures with a shared grid of nodes to obtain desired values of Poisson's ratios and Young's moduli. Through this scheme, deformation properties can be easily set piece by piece and 3D printed in useful combinations. For example, such nodally integrated tubular lattice structures undergo worm-like peristalsis or snake-like undulations that result in faster speeds than the monophasic counterpart in narrow channels and in wider channels, respectively. In a certain scenario, the worm-like hybrid metamaterial structure traverses between confined spaces that are otherwise impassable for the isotropic variant. These deformation mechanisms allow us to design shape-morphing structures into customizable soft robot skins that have improved performance in confined spaces. The presented analytical material design approach can make metamaterials more accessible for applications not only in soft robotics but also in medical devices or consumer products.

1. Introduction

The demand for complex and advanced material property needs in various applications has necessitated the development of novel functional materials. Recent advances in rapid prototyping and additive manufacturing[1–5] have brought solutions for fabrication of architectured materials, thereby the number of studies on mechanical metamaterials have shown a significant increase. Metamaterials have been described as engineered materials with such properties that are rare or non-existent in the nature,[6] and they are generally formed as patterns, which consist of repeated cellular geometries.[7,8] These cells may be folding patterns as in origami,[9,10] perforation patterns as in kirigami,[11,12] or structure geometry as in lattices.[13,14] Mechanical metamaterials are engineered materials of which mechanical properties primarily originate from their unit geometries and their mechanical properties can be customized without modifying chemical properties.[15] Previous studies have investigated this concept for negative Poisson's ratio,[16–20] negative compressibility,[21–23] negative stiffness,[24] negative swelling,[25,26] elastic hysteresis,[27] snapping deformations,[28] out-of-plane deformation through 3D design of architectured metamaterials,[29] and programmability.[30–32]

Programmability is a unique feature of mechanical metamaterials, which is realized by adjusting local mechanical properties via tuning geometrical parameters. Previous studies used programmability of mechanical metamaterials to create stiffness gradient,[33] to control energy absorption characteristics[34], and also to obtain shape-morphing characteristics by adjusting geometrical parameters in order[35–37].

Lattice metamaterials enable designers to create materials with desired mechanical properties. These mechanical properties originate from the deformation mechanisms of their cellular structures. These mechanisms may provide Poisson's ratios beyond the theoretical limit of continuum materials.[13,38] The most well-known lattice metamaterial is honeycomb pattern, which has a positive Poisson's ratio. The analytical mechanical model of honeycomb has been studied and the deformation characteristics of its unit structure have been described as the combination of flexure, stretching, and hinging.[13,38]

Y. Dikici, H. Jiang, B. Li, K. A. Daltorio, O. Akkus
Department of Mechanical and Aerospace Engineering
Case Western Reserve University
Cleveland, OH 44106, USA
E-mail: oxa@case.edu

Y. Dikici
Department of Mechanical Engineering
Bartin University
74100 Bartin, Turkey

O. Akkus
Department of Biomedical Engineering
Case Western Reserve University
Cleveland, OH 44106, USA

O. Akkus
Department of Orthopaedics
University Hospitals Cleveland Medical Center
Cleveland, OH 44106, USA

The ORCID identification number(s) for the author(s) of this article can be found under https://doi.org/10.1002/adem.202101620.

**ADVANCED
SCIENCE NEWS**

www.advancedsciencenews.com

**ADVANCED
ENGINEERING
MATERIALS**

www.aem-journal.com

Materials that have a negative Poisson's ratio are called auxetics,[7,16–20,39–41] examples of which include origami-based,[42] kirigami-based,[43] re-entrant,[13,38] chiral[14] models among others. Even though the reentrant honeycomb models,[16] which is a concave variation of conventional honeycomb, was studied more among cellular structures, chiral models are also well-known among the auxetic lattice structures. Unit cell geometries of chiral models consist of a node, generally in circle or square shape, and ligaments connecting units.[16]

Combining auxetic and the non-auxetic lattices (AnAs) rationally may expand the design possibilities of shape-morphing structures and enable new applications that take advantage of local variations in material properties. However, while previous studies have shown that (AnAs) can be combined thanks to geometrical similarity and hybridization compatibility (e.g. for shape-matching,[44] to achieve zero Poisson's ratio),[45] those studies were limited to only reentrant and conventional honeycomb patterns, and wider application, such as soft robotics, may require benefiting the advantages of other types cellular structures with variety of deformation mechanism. For instance, chiral models may offer options of isotropic, shear, or twist deformation modes,[46,47] and nodal component of the unit structures may provide easiness for practical applications.

This study developed an easy-to-implement, computationally inexpensive, and analytical approach to systematically combine AnAs that enables parametric design and modular construction of metastructures with nodal patterns. The developed analytical scheme was implemented for creating AnA tubes of which auxetic and non-auxetic phases were programmed to generate the same magnitude of expansion and contraction under loading. Shape-morphing characteristics of variety of combination have been studied via finite element analysis (FEA) and mechanical testing, and the differences of design approaches for computational and experimental models were investigated. A proof-of-concept application has been demonstrated as crawling soft robot skins by using 3D-printed AnA tubes. The robots with AnA skins showed worm-like peristalsis or snake-like undulation motions under simple uniaxial actuation, depending on combination configuration of auxetic and non-auxetic phases. This study shows that these motile structures with periodic shape-morphing characteristic improve the performance of biomimetic soft robots and may initiate new applications in the future. In addition to robotics, biomedical applications such as stents or manufacturing applications such as grippers can be derived from the approach that is presented herein.

2. Design Procedure

We aim to connect AnAs over space continuum. Spatial connectivity between two different lattice structures as such necessitates the geometrical spacings of the unit cells of the two lattices to be compatible. Furthermore, connectivity also necessitates that the unit cells have mutual geometrical features via which unit cells are grafted together. In this study, we chose anti-tetrachiral pattern[14,48] with square-shaped nodes as the auxetic phase of AnAs and used their nodes as connecting elements with the non-auxetic phase (**Figure 1**). In previous studies, nodes were defined as the circular, polygonal, or elliptical features of the
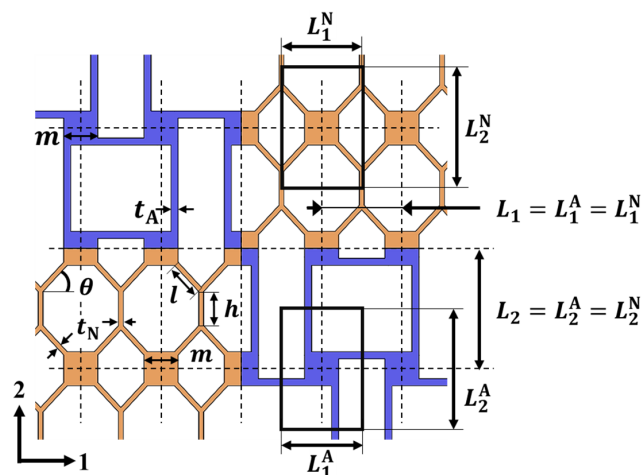
Figure 1. The nodal honeycomb pattern (orange) is compatible for in-plane combinations with the anti-tetrachiral pattern (blue) because both have nodes (at intersections of dashed lines), which is a mutual geometric feature in both cell structures. The unit cell boundaries are centered at the nodes as highlighted with black frames. Each rectangular grid piece defined by dashed lines can be modularly replaced with either the anti-tetrachiral or the nodal honeycomb pattern.

chiral cellular geometries.[14,47,48] While anti-tetrachiral cellular structure has this geometrical component, none of the non-auxetic patterns that are present to date has nodes. Therefore, we developed "the nodal honeycomb" pattern, which is a modified version of conventional honeycomb.[13,38] Through creation of nodal honeycomb, it become possible to execute a rational design procedure for combinations of anti-tetrachiral and nodal honeycomb lattices (Figure 1). Mathematical models explaining the deformation of these cellular structures are explained in more detail in Appendix 1 and 2.

Hybridization of two different patterns requires design principles for geometric and mechanical integration. The first design principle of our procedure is that the auxetic and non-auxetic units must be spatially matched such that the nodes overlap. In other words, the cellular size of both unit structures, thereby, distance between nodes must be equal.

$$L_1^A = L_1^N \tag{1}$$

$$L_2^A = L_2^N \tag{2}$$

A user-defined constraint is setting the Poisson's ratio values of both lattice structures to be equal in magnitude. This constraint provides a symmetric basis for deformations of auxetic and non-auxetic phases. In different iterations, this constraint can also be defined as different Poisson's ratio values for the two lattices to obtain asymmetry. For the sake of demonstration, we will limit the analysis to symmetric Poisson's ratio values for the two phases.

$$\nu_{21}^A = -\nu_{21}^N \tag{3}$$

The third principle is that the Young's moduli for both patterns will be equal to distribute the applied displacement in each

section equally, and to generate the same amplitudes of expansion or contraction for the auxetic and non-auxetic phases.

$$E_2^A = E_2^N \tag{4}$$

The mathematical procedure based on these principles first takes predefined geometrical parameters (m, l, h, t_N in Figure 1) to calculate the value of the inclined rib, the angle θ by using Equation (3). Poisson's ratios of unit cells are proportional to ratios of unit cells' lengths to their widths (Equations (A9) and (A16)); thus, Equation (3) can be expressed as

$$\frac{L_2^A}{L_1^A} = \frac{L_2^N}{L_1^N} \frac{-\cos\theta\sin\theta\left(-\frac{1}{K_f} + \frac{1}{K_s} - \frac{1}{K_h}\right)}{\frac{\cos^2\theta}{K_f} + \frac{\sin^2\theta + (h/l)}{K_s} + \frac{\cos^2\theta}{K_h}} \tag{5}$$

where K_f, K_s, and K_h represent the stiffness values that are associated with flexure, stretching, and hinging of ligaments that are connecting the nodes, respectively. Because of spatial-matching criteria (Equations (1) and (2)), the Equation (5) is simplified to

$$\frac{-\cos\theta\sin\theta\left(-\frac{1}{K_f} + \frac{1}{K_s} - \frac{1}{K_h}\right)}{\frac{\cos^2\theta}{K_f} + \frac{\sin^2\theta + (h/l)}{K_s} + \frac{\cos^2\theta}{K_h}} = 1 \tag{6}$$

The value of θ that is satisfying Equation (6) provides the Poisson's ratio symmetry.

The last geometrical parameter is determined by solving Equation (4) for ligament thickness of anti-tetrachiral lattice, t_A (Equation (A10) and (A18)).

Geometrical parameters and Young's modulus are normalized to be represented in the nondimensional form as (**Figure 2**)
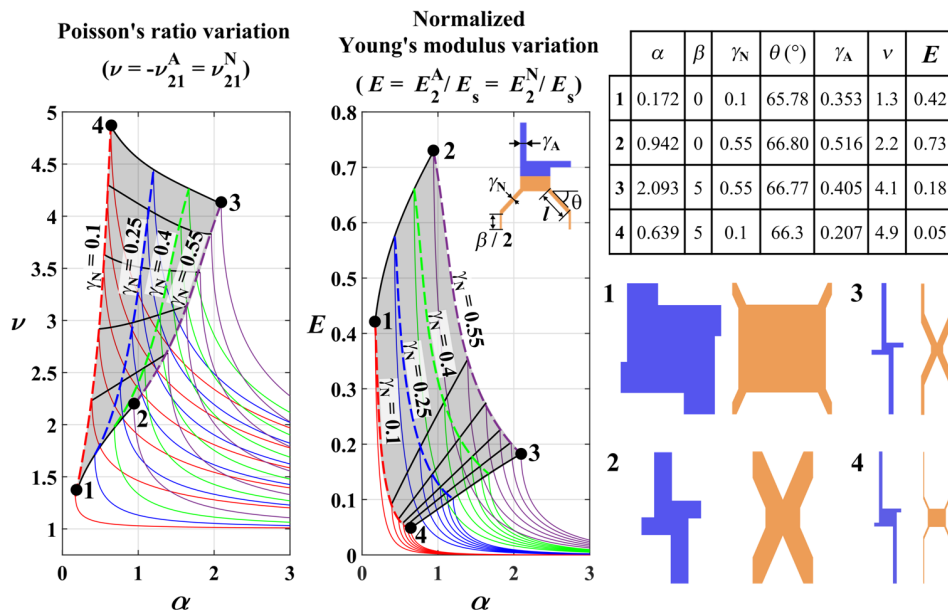
$$\alpha = \frac{l}{m} \tag{7}$$

$$\beta = \frac{h}{m} \tag{8}$$

$$\gamma_N = \frac{t_N}{m} \tag{9}$$

$$\gamma_A = \frac{t_A}{m} \tag{10}$$

$$E = \frac{E_2}{E_s} \tag{11}$$

The analytical scheme is helpful for easy and rapid surveying the high degree-of-freedom geometric space. Via this procedure, unit geometries for desired spatial and mechanical properties can be selected and used in computational and experimental studies. The Poisson's ratio and Young's modulus were plotted with respect to α for multiple β and λ_N values to have a better understanding of nonlinear mechanical effects of predefined geometrical parameters (Figure 2). The results demonstrates that vertical ligament length (β) has greater influence on Poisson's ratio (Figure 2a,c), while ligament thickness (λ_N) has greater influence on Young's modulus (Figure 2b,c). Since increasing β is not a theoretical limitation, no maximum value can be determined for Poisson's ratio mathematically. In contrast, there are geometric constraints limiting increasing Young's modulus. Since the ligament thickness can be increased until it can have the form of the nodal honeycomb geometry shown as model 2

	α	β	γ_N	$\theta\,(°)$	γ_A	v	E
1	0.172	0	0.1	65.78	0.353	1.3	0.42
2	0.942	0	0.55	66.80	0.516	2.2	0.73
3	2.093	5	0.55	66.77	0.405	4.1	0.18
4	0.639	5	0.1	66.3	0.207	4.9	0.05

Figure 2. Effects of geometrically and mechanically integrated unit cell geometry on mechanical properties are demonstrated. a) Poisson's ratio and b) normalized Young's modulus variations were plotted with respect to α for multiple β and λ_N values (solid and dashed lines, respectively). Lines in shaded areas define the maximum value points of all curves that are theoretically possible. The results indicate that vertical ligament length (β) has greater influence on Poisson's ratio, while ligament thickness (λ_N) has greater influence on Young's modulus. The geometric parameter combinations that defined c) the maxima of mechanical parameters (1, 2, 3 and 4) are tabulated, and d) schematically depicted in terms of corresponding lattice shapes.

**ADVANCED
SCIENCE NEWS**

www.advancedsciencenews.com

**ADVANCED
ENGINEERING
MATERIALS**

www.aem-journal.com

(Figure 2d), this model has the highest possible Young's modulus value of AnA concept (Figure 2c).

As results indicated, the ranges of mechanical properties are theoretically large; however, there are practical limitations to consider for applications. Since unit cells with high Poisson's ratio have geometries with high aspect ratio, the required fabrication space becomes larger. In other words, manufacturing equipment with high resolution (3D printers, laser cutters, etc.) is needed to build these metastructures in limited spaces. Furthermore, high aspect ratio structures may be instable for buckling under compression, which is another limitation for compression necessitating applications. These should be considered in design optimizations.
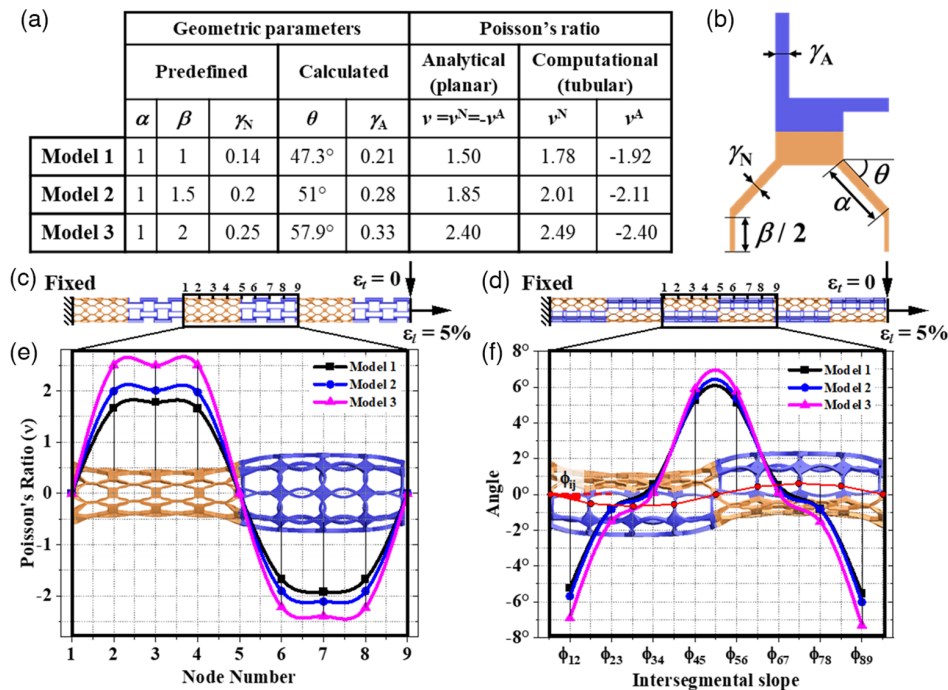
3. Tubular AnA Configurations as Expansional and Flexural Metastructures

For the purpose of converging to metastructures that display peristalsis-like (expansional) and snake-like (flexural) deformation patterns, auxetic and non-auxetic phases were assembled as illustrated in **Figure 3**. We visualized the deformation patterns of tubular arrangements of AnA metastructures using FEA (FFEPlus solver, Static mode, SolidWorks 2019) and analyzed three models with different dimensional parameters (Model 1, 2, and 3 in Figure 3). Geometric models were first designed in SolidWorks as flat, and then rolled into tubes using the flex

feature. Tubular metastructures had fully fixed boundary condition on one end whereas the other end underwent a prescribed displacement resulting in 5% elongation on the longitudinal axis ($\varepsilon_l = 5\%$). Transverse movement on the longitudinally deforming end was confined ($\varepsilon_t = 0$) (Figure 3c,d). The AnA tubes were meshed with high-quality solid mesh of tetrahedral elements with 5% tolerance. Although the thermoplastic polyurethane (TPU) is a nonlinear material, we defined it as a linear elastic material with a Young's modulus value of 26 MPa because the applied strain of 5% is well within the yield strain of TPU at 55%.[49]

Expansional AnA (e-AnA) resulted from alternating repetitions of non-auxetic nodal honeycomb segments and auxetic anti-tetrachiral segments (Figure 3c). Each segment consisted of four unit cells ($4 \times L_2$) along the longer axis of the tube, and eight units along the circumference ($8 \times L_1$). FEA simulation confirmed the expected peristalsis-like deformation pattern where segments alternatingly expanded or contracted under uniaxial extension (Figure 3e).

Flexural AnA (f-AnA) was obtained by a checkerboard arrangement of auxetic and non-auxetic phases. One half of each segment was auxetic with four-section long ($4 \times L_2$) and four units along the arc ($4 \times L_1$) whereas the other half was non-auxetic with the same repeat number of unit cells. In consecutive segments, auxetic half of one segment grafted with the non-auxetic phase of the next segment. In line with the postulation, f-AnA tubular metastructure underwent

	Geometric parameters				Poisson's ratio		
	Predefined			Calculated		Analytical (planar)	Computational (tubular)	
	α	β	γ_N	θ	γ_A	$v = v^N = -v^A$	v^N	v^A
Model 1	1	1	0.14	47.3°	0.21	1.50	1.78	-1.92
Model 2	1	1.5	0.2	51°	0.28	1.85	2.01	-2.11
Model 3	1	2	0.25	57.9°	0.33	2.40	2.49	-2.40

Figure 3. Finite element analysis (FEA) was used to visualize deformation patterns of tubular metastructures for a) various lattice cell geometries (Models 1–3) of which normalized parameters are illustrated on b) an interphase cell geometry. Auxetic (blue) and non-auxetic (orange) phases were designed parametrically and combined to create c) expansional auxetic and non-auxetic lattices (e-AnAs) and d) flexural AnAs (f-AnAs). The middle phases of uniaxially deformed tubes were analyzed to quantify the deformation of e) e-AnAs and f) f-AnAs and their variations between different lattice models. Bending behavior of f-AnAs is reported in terms of intersegmental slope f), which is the angle between the longitudinal axis of the undeformed structure and central line of the deformed body. Greater amount of expansion–contraction and bending is observed with increasing Poisson's ratio.

periodic bending under uniaxial deformation. Both e-AnA and f-AnA tubes were designed as six longitudinally connected segments with a pattern thickness of 2 mm.

The data representing the displacement on the transversal plane were collected from the central points of the nodes at only middle sections to minimize the boundary effects (Figure 3c,d). The amount of expansion of nodal cross sections was divided by the diameter of the undeformed tube to calculate transverse strains. Poisson's ratios were calculated as the negative value of the ratio of strains in transverse and longitudinal axes. Poisson's ratio variations of the AnA were determined by repeating the calculation for each nodal cross section. Although, shape morphing of e-AnA can be expressed as Poisson's ratio variation because the material deformation under loading is concentric throughout the longitudinal axis (Figure 3a,b), the deformation characteristic of f-AnA is not compatible for this quantification with Poisson's ratio. This is because both expansion and contraction modes are present in each cross section of f-AnA; therefore, the deformation was expressed as the intersegmental slope, which is the angle between the central line in deformed structure and longitudinal axes of undeformed structure (Figure 3c,d).

FEA results demonstrate that the geometrical parameters obtained from the analytical approach provide approximately equal (within 8%) amplitudes of lateral expansion and contraction in auxetic and non-auxetic phases of e-AnA. The difference between analytically and computationally determined Poisson's ratios of e-AnAs decreases in high Poisson's ratio values. While previous metamaterial computational results have been improved to match computational results and analytical predictions,[14,50] here we observe greater differences because of the periodically changing boundary conditions between sequential phases. Also, because the lattices are designed flat and then wrapped into a tubular shape, the effective lengths in the radial direction are related to chord lengths, which are less than the designed lengths along the circular arc, which increases the aspect ratio and thus the Poisson's ratio. Therefore, in Model 3, which has the longest distance between boundaries, the Poisson's ratio is measured at the center approach of the analytical result. In e-AnA and f-AnA, the amplitude of expansion/contraction and bending (respectively) can be controlled by changing the Poisson's ratio through adjustment of the geometric properties of unit lattices.

4. Manufacturing and Experimental Evaluation of AnA Tubes

Advancements of desktop 3D printers have provided easy fabrication tools for complex geometries; however, their capabilities are still limited for designs with thin and detailed geometrical features and designers may require to find pragmatic solutions to improve the product quality. Such an issue may be experienced on fabricating tubular lattice structures. Therefore, in this study, AnAs have been fabricated in planar form (**Figure 4**a) and then rolled into tubes (Figure 4b). Instead of using one of the models performed in computational study, a smaller model was designed because of the limited build area of 3D printer used (Ultimaker S3, Ultimaker, Zaltbommel, the Netherlands). The model, which was built with Ultimaker TPU 95 A, was designed
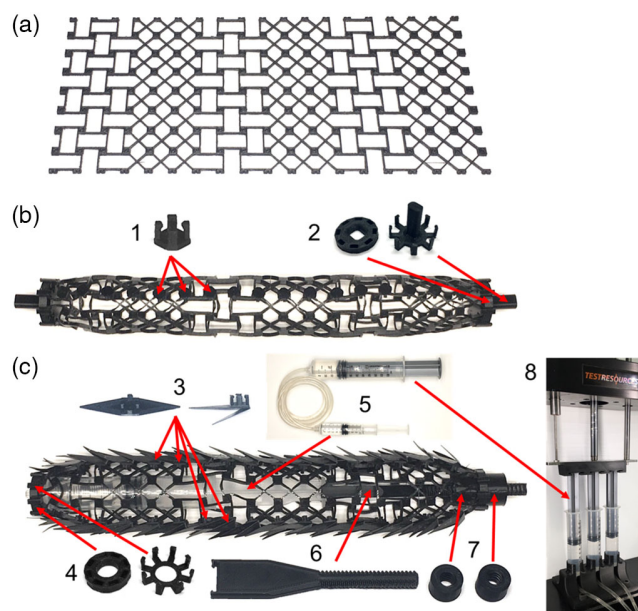

Figure 4. a) The designed lattice structures have been fabricated in planar form, and rolled into tubes using a set of custom-designed snap connectors 1) to maintain the tubular form by holding nodes on the long edges together. b) The parts placed at the ends of tubes 2) both fixed the nodes and provided place to be gripped by the clamps of the test machine. c) To attain frictional anisotropy with the terrain, snap connectors for motility test samples were designed with triangular extensions 3). They were 3D-printed as flat and one of the extensions was folded to obtain unidirectional movement and placed on the seam and lateral nodes. Components shown with number 4 enabled to fix the nodes at ends and to assemble the actuation mechanism in the lattice tube. Actuation was carried out via a water-filled syringe–tube–syringe system 5). Small syringe was placed in the tube, and its movement was transferred to the front and with a screwed rod 6) and end two bolts 7). The large syringe was placed on the test mechanical test machine 8), which was used converted to a syringe pump c).

with six longitudinal sections, each of which is of three-unit long and has eight units along the circumference (Figure 4a).

Mechanical snap connectors (1 in Figure 4b), which join the nodes along a seam, were designed and 3D printed with a hard material (Ultimaker Tough PLA) to maintain cylindrical shape. Another apparatus was designed to close the ends of the tubes and to be gripped by the test machine (2 in Figure 4a).

Since the design procedure of the fabricated model is not the same with analytical and computational models, we conducted mechanical tests to investigate the effect of the design differences (**Figure 5**). We prepared three sets of auxetic, non-auxetic, e-AnA, and f-AnA samples, and placed markers on the lateral nodes of the two phases, located in the middle of the tubes (Figure 5b). Samples were placed on a mechanical test machine (Test Resources 800LE3-2; Test Resources Inc., MN) and a camera has been placed 1.5 m away from the samples. Photographs were taken at the original designed position (Original in Figure 5b), and after being deformed in tension to a level of ≈5% strain (deformed in Figure 5b). Marker positions were digitized by using an image analysis software (NIH, ImageJ). Poisson's ratio for concentrically deforming lattices (Figure 5c) and
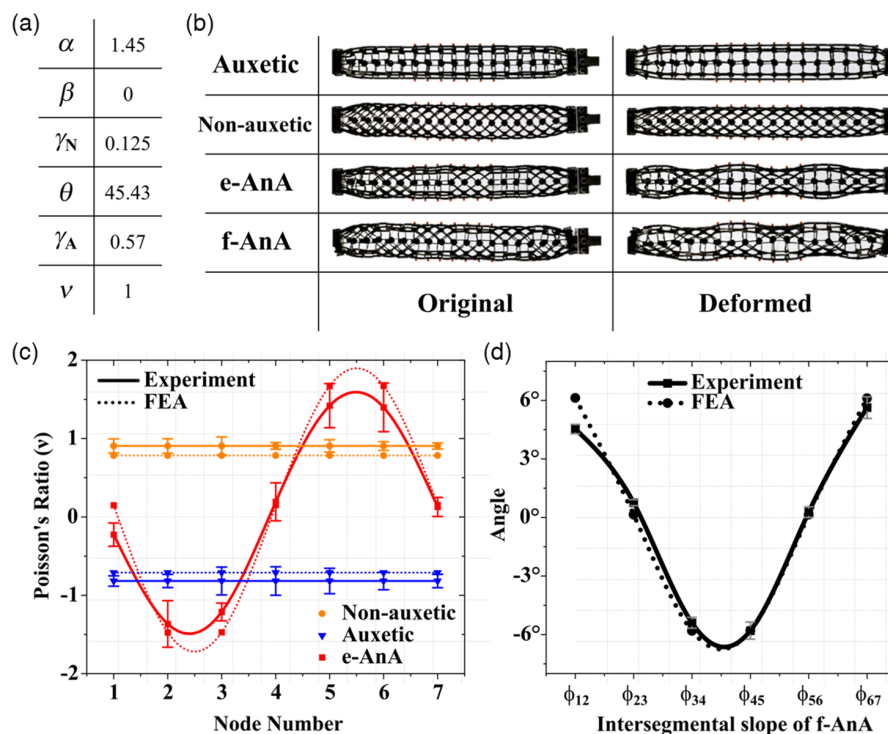
Figure 5. Experiments were conducted to compare the design differences with computationally investigated models. a) The lattices designed with the same geometrical parameters were 3D printed with Ultimaker thermoplastic polyurethane (TPU) and b) a displacement resulting in 5% strain was applied. c) By generating approximately equal amount of shape changing with a 6% difference in auxetic and non-auxetic phases of e-AnA, the experiment fulfilled the aim to generate close magnitude of expansion–contraction in both lattices. d) Furthermore, the design differences cause a negligible effect in bending of computational and experimental f-AnA models. Error bars stand for standard deviation.

intersegmental slope for f-AnA (Figure 5d) were calculated by using the collected marker data via the same method with computational analysis.

Rolling the flatly fabricated metastructures into tubes causes a lateral contraction. This contraction results in an axial elongation for non-auxetic lattices and an axial shortening for auxetic lattices. To eliminate this effect and to match the length of tubes with the configuration in their FEA counterpart, the in-plane lengths of the structures were taken as reference and structures were preloaded to keep them at the same lengths (Original in Figure 5b) before loading (Deformed in Figure 5b).

While others have shown the accuracy of FEA in modeling deformations for honeycomb[50] and anti-tetrachiral lattices,[14] to our knowledge, the effects of wrapping the lattice into a tube have not previously been experimentally studied. The experimental Poisson's ratio is 87% of FEA results for non-auxetic, 94% for auxetic. The agreement suggests that flat lattice structures can be conveniently printed flat and then folded into 3D shapes with desired Poisson's ratios. This is a promising alternative to the challenges of directly 3D-printing lattices in cylindrical form without changing deformation properties.

Furthermore, we validate the modularity of these spatially matched lattice sections by conducting these same experiments with e-AnA and f-AnA configurations. Experimental predictions are within 88% of FEA for e-AnA and 96% for f-AnA. Taken together, the modularity, analytical approximations, and ease of fabrication make these AnAs accessible for broader applications, such as new soft robotic devices. Furthermore, the agreement between experimental and computational analyses implies that different shape-morphing lattice combinations can be surveyed computationally to identify suitable geometries for a defined outcome, to reduce the design space prior to the implementation of time-consuming manufacturing.

This study shows that the nodes can be used to connect surfaces to each other (e.g., here to form a tube). The flat lattices can be stitched together like squares in a quilt and then deformed into 3D spaces. This makes AnA metamaterials more accessible to potential users—either with novel materials or novel applications. Different or similar phases can be snapped together with almost invisible seams. More importantly, the seams have little effect on overall behavior, as we showed with our experimental results. Custom skins with auxetic or non-auxetic "pixels" that open, tighten, or loosen at particular spots could be valuable in mechanism design, wearables, or packaging.

5. Motile Robots with AnA Skins

The ability of AnAs to generate multiple deformation modes may be highly promising for use in many applications. Especially, having dynamic shape-morphing characteristics may improve compliance to the environment, the speed performance as well

**ADVANCED
SCIENCE NEWS**

www.advancedsciencenews.com

**ADVANCED
ENGINEERING
MATERIALS**

www.aem-journal.com

as the ability to move in confined spaces. Moreover, the analytical design concept which enables to tune the Poisson's ratio may help to optimize the shape-changing amplitudes for specific spatial requirements. Poisson's ratio is especially critical for worm-like crawling in an idealized model, the greater the Poisson's ratio, the more efficient the robot.[51] We have previously shown how mechanisms with an effective Poisson's ratio of 1.5 enable segments to both advance and anchor.[52] Others have shown that AnAs can be added to inchworm robots to enable alternating engagement and detachment.[53,54] Here, we present how using AnA lattices as skins can improve the motility of soft robots (**Figure 6**, and VideoS1, Supporting Information). As an illustration of the capabilities of the AnAs, we focused on channels with varying widths to simulate different types of tunnels or burrows where soft animals are particularly adept in navigating.

The motile structures were created with the same AnA structures and isotropically deforming non-auxetic lattice designed for mechanical testing. The addition of triangular scales (made of Ultimaker Tough PLA), akin to parapodia on some worms or scales on snake-inspired kirigami,[55,56] to the lateral nodes provided the frictional anisotropy (3 in Figure 4c). The nodes at the longitudinal ends of the tubes were assembled to an apparatus, which enable actuation mechanism to be placed in the lattice tube (4 in Figure 4c).

To move the motile structures, a hydraulic system was prepared to actuate both of AnAs and non-auxetic lattice simultaneously. This system consists of the mechanical test machine and three water-filled syringe–tubing–syringe mechanisms (5 and 7 in Figure 4). Three large syringes (60 mL) were placed on the mechanical test machine and the small syringes (10 mL) on the other ends of the tubes were assembled in the lattices between its ends to generate uniaxial loading. We programmed the test machine to generate periodic contraction and tension in a 12 mm range with the feed rate of 3 mm s^{-1},
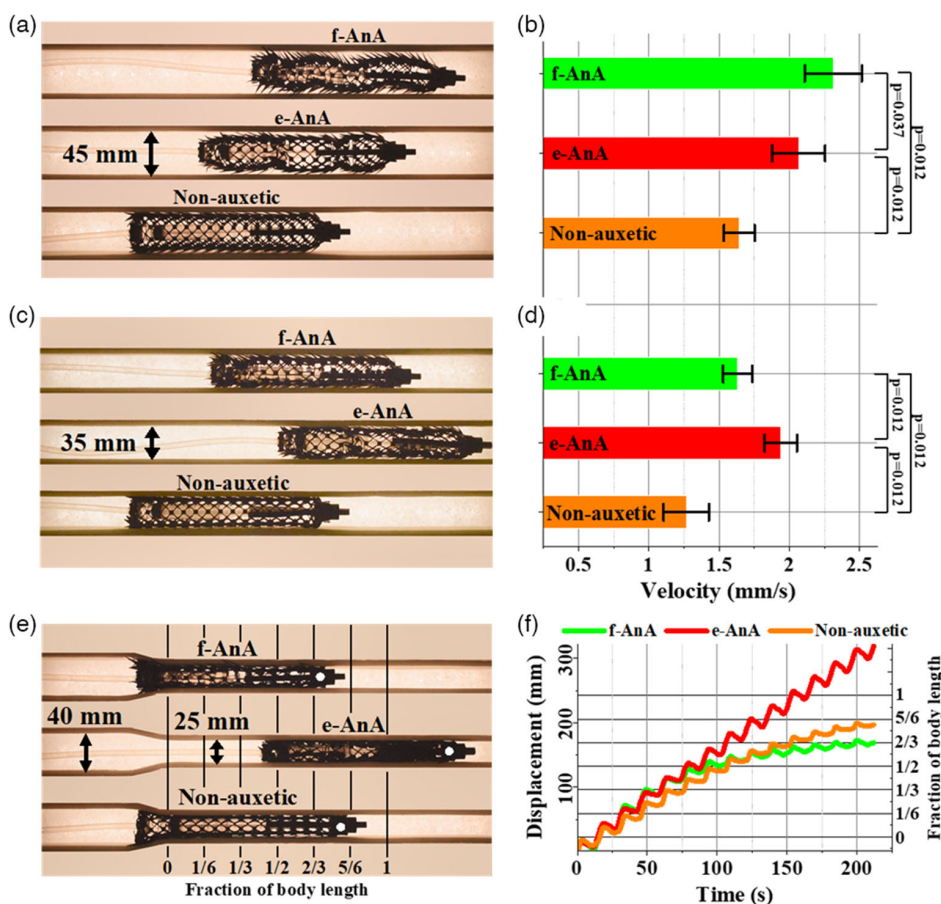
Figure 6. AnAs enable improved locomotion through confined spaces such as these three channels. In each of three types of channels, three metamaterial tubes (f-AnA in green, e-AnA in red, and non-auxetic in orange) are controlled in parallel with the same hydraulic pressure source, which longitudinally extends and contracts the tubes periodically. Scale-like extensions placed on lateral nodes and foam-covered channel walls create frictional anisotropy. In the widest channels, a) at 45 mm wide, f-AnA has the best motility (see Video S1, Supporting Information) and b) overall speed. In narrower channels c) at 35 mm wide, d) e-AnA is fastest. Error bars show standard deviation. P-values of Kruskal–Wallis test are 0.003 for 45 mm wide channel and 0.002 for 35 mm wide channel. P values in the figure are results of Mann–Whitney tests ($N = 5$). If the channel becomes even more confined, as shown in the e) narrowing, e-AnA keeps moving while the others gradually decrease in f) progress per cycle until stalling at the instant shown with e). Note that the starting positions of the tubes were such that they reached the beginning of the narrowing (Line zero) after one cycle. Lines represent the displacement of white markers (the front end of the lattice), which are numbered with the fraction of the length of the tube in the narrow channel. Original length of the tubes is 220 mm.

and 1 s of wait at extremum points. The motile structures which were assembled and connected to the actuation system were placed in the channels, which were covered with 5 mm thick foam sheets to improve the frictional anisotropy.

The lattices were tested for three test cases: 1) 45 mm channel width, 2) 35 mm channel width, and 3) narrowing channel (from 40 to 25 mm). The movements of robots were recorded in five replicates for each case from top view with a camera. Markers were placed at the tip of the robots and data were collected. Recorded videos were analyzed by a commercial software (Photron FASTCAM Viewer). Significant differences between the velocities of motile structures were tested by using a nonparametric Kruskal–Wallis test, and post hoc pairwise comparisons were performed by using Mann–Whitney U-test. Significance was reported at the level of $p < 0.05$ as shown in Figure 6.

Results showed that when the channel width is 1.3 times larger than the diameter of the metamaterial tube (45 mm), the f-AnA metamaterial structure moves faster than (12%) e-AnA and (41%) isotropic non-auxetic structures (Figure 6a,b, and Video S1, Supporting Information). In contrast, the e-AnA structure showed better motility (19% faster than f-AnA and 53% faster than non-auxetic lattice) in smaller channels with width (35 mm) approximately equal to the metamaterial tube diameter (32 mm not including scales) (Figure 6c,d, and Video S1, Supporting Information). In both types of channels, the non-auxetic robot was the slowest. These results emphasize that periodic shape morphing of AnA may enable soft robots to test strain patterns observed in animals, which can improve the performance of biomimetic soft robots in the future.

Furthermore, AnA tubes can address a "bottleneck challenge," in which the channel gets narrower than the metamaterial tube radius along the path of motion. We have previously shown such a challenge can be addressed by complex control of different segments.[57] Here, we show that the e-AnA configuration can smoothly transition in response to the channel width without changing velocity passively without the need for active control. We start all three configurations in a channel with intermediate width (40 mm), such that all three can locomote. Propelled by contact with the channel walls, all three can enter the narrowing. However, only the e-AnA structure continues to travel within the narrowing, while the f-AnA and non-auxetic structures become jammed and cannot progress when the ≈4-section-long part remains in the wider channel (Figure 6e,f, Video, S1, Supporting Information). The success of e-AnAs is due to the fact that the metamaterial phases within the narrowing continue to expand and contract, gaining purchase via the frictional anisotropy. In contrast, f-AnA does not change its diameter as much (total Poisson's ratio ≅ 0). While the isotropic structure can expand and contract (total Poisson's ratio ≅ +0.9), it can do so only in unison along its length. Thus, in highly confined spaces, Poisson's ratio that varies along the length (such as between −1.4 and +1.4 for e-AnA) is uniquely valuable for motility.

Here, we have shown the advantages of combining auxetic and non-auxetic patterns in a grid-like configuration for soft robotics —AnAs have better motility than isotropic materials in confined channels. Specifically, e-AnA embodies in one matrix the balance of expansion, and contraction that we previously hypothesized is required by a series of peristaltic muscle activations.[51,52,57] As a result, e-AnA deforms more evenly in confined tubes. In contrast, isotropic lattices demonstrate localized deformation (aka jamming), and thus traverse confined spaces less well. These materials enable scalable solutions to established locomotion challenges such as transitioning through a bottleneck that would otherwise limit worm-like and snake-like soft robots. Such robots can have application in accessing buried infrastructure, medical stents and implants, etc. However, this is just one example. These simple lattice frameworks can also facilitate broader use of bending actuator concepts[58,59] and other customized metamaterials yet to be conceived.

6. Other Considerations

AnA surfaces can also be overlaid or stacked by joining the nodes to enable out-of-plane deformation or stiffening. We show this computationally in **Figure 7**. If an auxetic layer and a non-auxetic layer are stacked in a z-AnA configuration and connected with pins, out-of-plane (z-direction) protrusions emerge for in-plane axial loading. In contrast, symmetrically stacked auxetic and non-auxetic structures (A–N–N–A or N–A–A–N) produce an order of magnitude higher longitudinal stiffness than combinations of single-type isotropic lattices (A–A–A–A or N–N–N–N) (Figure 7b). This outcome supports the conclusions of a previous computational study in which auxetic and non-auxetic
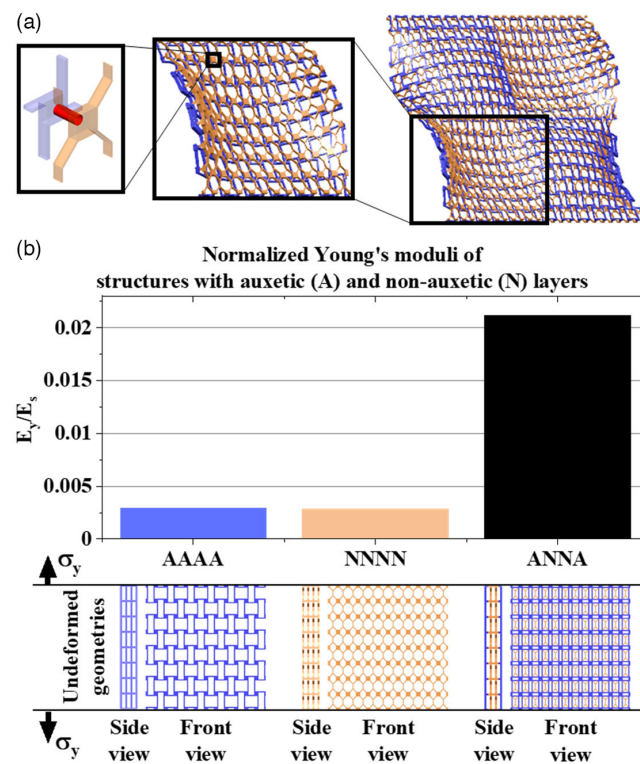
Figure 7. Nodal AnAs were combined in out-of-plane stacking configurations with the geometrical parameters given as Model 1 in Figure 3a and investigated via FEA. Results show that a) z-AnA takes a wavelike shape bulging at the auxetic side under uniaxial tension. Simulations also demonstrate that b) symmetrically stacked auxetic and non-auxetic layers have higher (for this case, 7.4 times higher) Young's modulus than monophasic structures.

**ADVANCED
SCIENCE NEWS**

www.advancedsciencenews.com

**ADVANCED
ENGINEERING
MATERIALS**

www.aem-journal.com

combinations were modeled as continuum materials.[60] The source of this increasing stiffness originates from the opposite flow of metamaterials in neighboring layers under loading. Being able to induce different stiffnesses and 3D deformations enables finer biomimicry at scales smaller than actuators, for example, to create load-sensitive fingerprint ridges, to define creases for folding, or to dynamically vary friction of feet.

7. Conclusions

A primary contribution of this work is the rational design of AnAs—metamaterials with combined auxetic and non-auxetic phases in a single lattice. Prior to this work, auxetic and non-auxetic combinations were limited to conventional honeycomb and reentrant lattices. Our work enables the use of different auxetic patterns (specifically anti-tetrachiral which had no previously established application) and introduces the first non-auxetic nodal pattern (nodal honeycomb). Modular grids are created with nodal honeycomb and anti-tetrachiral unit cells (Figure 1). The unit cell geometry is designed with our analytical relationships for symmetric deformation ($-\nu^A = \nu^N$) and matching mechanical ($E^A = E^N$) properties (Figure 2). AnA metamaterials with periodic Poisson's ratio variation were demonstrated computationally (Figure 3) and experimentally (Figure 5). AnAs can generate spatial patterns of expansion–contraction (e-AnA) or flexure (f-AnA), which result in locomotion under periodic uniaxial loading (Figure 6).

Soft robotics has demonstrated the importance of soft continuum materials in mechanical design—but lattice metamaterials have long been underutilized. Young's modulus and Poisson's ratio are critical, but traditionally the designer has to limit the number of different materials used. Finely specifying different material properties at different points is a challenge, even with multi-material 3D-printing. Moreover, sometimes, stiff materials are selected for thermal, biological, electrical, or chemical compatibility. Being able to use fine lattices as mechanisms within mechanisms will be a tool that can enable selective softness in these materials. Yet, to our knowledge, anti-tetrachiral patterns have not been used in soft robotics. While honeycomb and reentrant patterns have been used in mobile robots,[53,54] we hope that here by showing that metamaterials quantitatively improve performance in a challenging environment will encourage further use of these types of materials in new and innovative ways—perhaps using our analysis to create multi-stiffness materials ($E^A \neq E^N$) for layer jamming,[61] smoothly varying Poisson's ratio within 3D-printable biomaterials, or design mechanisms that amplify local actuation with material-scale FEA.

In future work, our approach can be used to explore new combinations of nodal patterns. Other unit cell designs (e.g., hybrid[62] or a new nodal reentrant) can be incorporated following the same type of analysis. Unit cells can be chosen to have different combinations of properties ($E^A \neq E^N$, $\nu^A \neq -\nu^N$) using our equations. More than two unit cells can be combined in new patterns, for example, tetrachiral patterns to add twisting motions. The 3D geometries, which we have investigated with fixed connections between each node, enable even further variation with different types of connections. The shared nodes of these lattices create a grid that enables novel custom metamaterials with deformations that can be mechanically "programmed" piece by piece.

Appendix 1. Analytical Model of the Anti-Tetrachiral Unit Cells with Square Nodes

An analytical model for mechanical properties of anti-tetrachiral pattern with circular nodes was presented and later improved by Gatt et al.[14,48] (**Figure 8**). The original model[14] calculates Poisson's ratio and Young's modulus values of the anti-tetrachiral patterns, which have different thicknesses (t_1, t_2), lengths (l_1, l_2), and Young's moduli of parent materials (E_{s1}, E_{s2}) in horizontal and vertical ligaments. The improvement was made through adding the consideration of ligament–node connection and its effect on the effective bending length of ligaments.[48] The reported analytical model is as follows.

$$\nu_{ij} = -\frac{(2r + t_j)l_i}{(2r + t_i)l_j} \tag{A1}$$

$$E_i = \frac{1}{3(2r + t_i)^2}\frac{l_i}{l_j}\left(\frac{E_{s1}t_1^3}{l_1 - 2g_I} + \frac{E_{s2}t_2^3}{l_2 - 2g_I}\right) \tag{A2}$$

($i = 1, 2$ and $j = 1, 2$)

where r is the radius of the node, and g_I is the length of the ligament–node connection.[14,48]

We simplified the model by setting ligament thicknesses the same and by using single type of material.

$$t_A = t_1 = t_2 \tag{A3}$$

$$E_s = E_{s1} = E_{s2} \tag{A4}$$

Additionally, we used the considerations of the improved model to modify this analytical scheme to create a mechanical formulation for the pattern with square nodes with the edge length of m (Figure 8b). The modifications on the parameters are shown as follows.

$$g_I = r + t_A \tag{A5}$$
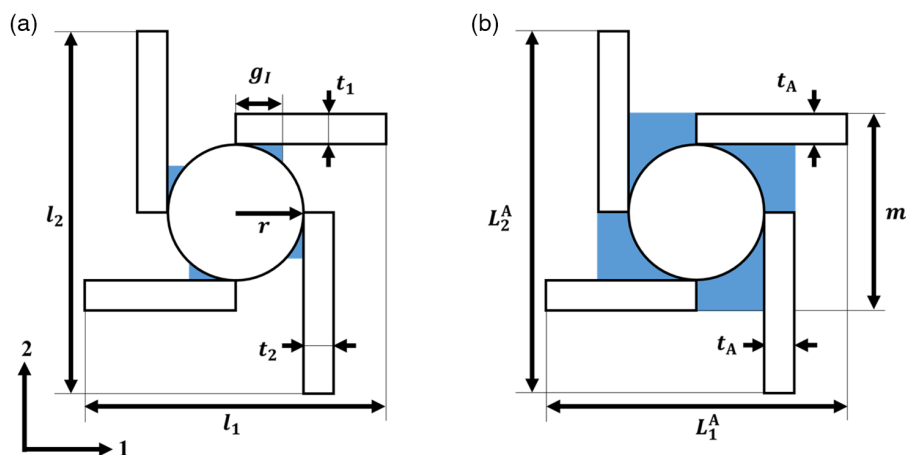
$$m = 2g_I \tag{A6}$$

$$L_1^A = l_1 \tag{A7}$$

$$L_2^A = l_2 \tag{A8}$$

The purpose of changing the notation in the Equation (A7) and (A8) is to eliminate the confusion with the inclined rib of the honeycomb pattern, which is addressed in the next section. After the simplifications and the modification, the resulting formulae appear as follows.

$$\nu_{ij}^A = -\frac{L_i^A}{L_j^A} \tag{A9}$$

$$E_i^A = \frac{E_s^A t_A^3}{3(m - t_A)^2}\frac{L_i^A}{L_j^A}\left(\frac{1}{L_1^A - m} + \frac{1}{L_2^A - m}\right) \tag{A10}$$

($i = 1, 2$ and $j = 1, 2$)

**ADVANCED
SCIENCE NEWS**

www.advancedsciencenews.com

**ADVANCED
ENGINEERING
MATERIALS**

www.aem-journal.com

Figure 8. Geometrical parameters of anti-tetrachiral pattern with a) circular nodes were converted to generate the pattern with b) square nodes.[48] Previous studies reported a realistic analytical model by considering the nature of the ligament node connection, of which length is shown as g_l a). The model with square node can be derived if this variable in the analytical model is set as the accumulation of the radius of the circle, r, and the ligament thickness, t_A. With this adjustment, ligament–node connection is assigned as the half length of the square node width, m b).

## Appendix 2. Analytical Model of the Nodal Honeycomb Unit Cell

Nodal honeycomb is a modified form of the conventional honeycomb (**Figure 9**a) that is obtained by introducing finite-sized square-shaped nodes (Figure 9b). Analytical modeling of the nodal honeycomb capitalizes on existing mathematical principles for the conventional honeycomb of which deformation is characterized by flexure,[13] stretching, and hinging[38] mechanisms. Combination of these three mechanisms with the consideration of effective ligament length has been previously shown to agree closely with FEA.[50] We defined the mathematical model of the nodal honeycomb pattern with the procedure that is similar to

that followed by previous studies.[13,38,50] As a difference, instead of defining additional effective length parameters like Grima et. al.,[50] we kept l and h as effective lengths and designed suitable ligament intersection geometry, which was assumed as rigid mathematically (Figure 9c). Therefore, horizontal (L_1) and vertical (L_2) size of the unit cell varies depending on the angle θ. Resulting mathematical model which defines Poisson's ratio and Young's modulus are expressed as follows.

For $0 \leq \theta \leq 30$

$$L_1^N = m + 2l\cos\theta + t_N[1 - 2\sin\theta] \tag{A11}$$

$$L_2^N = m + 2l\sin\theta + h \tag{A12}$$
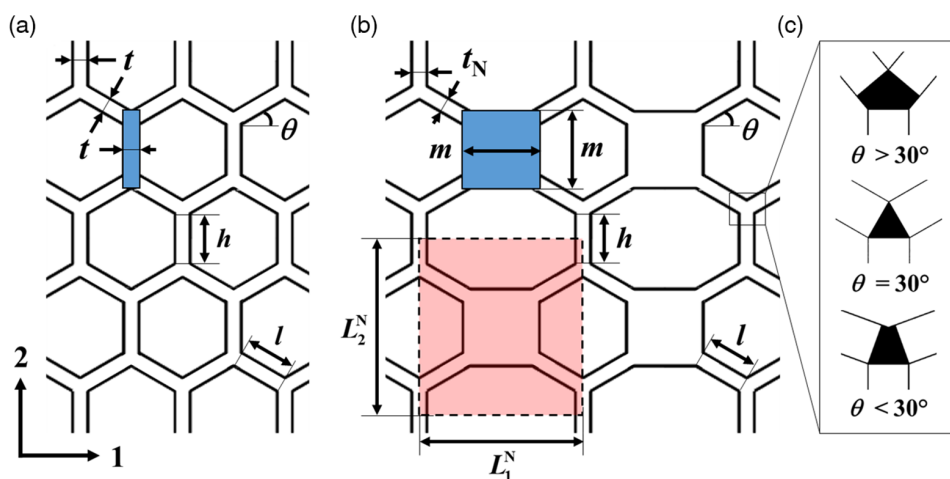
Figure 9. The non-auxetic pattern was derived from conventional honeycomb pattern. a) The geometrical parameters affecting mechanical properties of conventional honeycomb pattern were determined as shown in (b) The nodal honeycomb pattern was created by expanding the thicknesses of vertical ligaments demonstrated with the blue color on a) to form square-shaped nodes. The resulting unit geometry is shown with pink section in b). c) The ligament intersection geometry varies depending on the angle, θ, to ensure that the variables l and h fully represent the length of deforming ligaments. Ligament intersections shown with black color c) are assumed as rigid in the analytical model.

2101620 (10 of 12)

For $30 \leq \theta \leq 90$

$$L_1^{N} = m + 2l \cos \theta \tag{A13}$$

$$L_2^{N} = m + 2l \sin \theta + h + t_{N}[(2 \sin \theta - 1) \tan \theta] \tag{A14}$$

$$\nu_{12}^{N} = \frac{L_1^{N}}{L_2^{N}} \frac{-\cos \theta \sin \theta \left(-\frac{1}{K_f} + \frac{1}{K_s} - \frac{1}{K_h}\right)}{\frac{\sin^2 \theta}{K_f} + \frac{\cos^2 \theta}{K_s} + \frac{\sin^2 \theta}{K_h}} \tag{A15}$$

$$\nu_{21}^{N} = \frac{L_2^{N}}{L_1^{N}} \frac{-\cos \theta \sin \theta \left(-\frac{1}{K_f} + \frac{1}{K_s} - \frac{1}{K_h}\right)}{\frac{\cos^2 \theta}{K_f} + \frac{\sin^2 \theta + (h/l)}{K_s} + \frac{\cos^2 \theta}{K_h}} \tag{A16}$$

$$E_1^{N} = \frac{L_1^{N}}{L_2^{N}} \frac{1}{z} \frac{1}{\frac{\sin^2 \theta}{K_f} + \frac{\cos^2 \theta}{K_s} + \frac{\sin^2 \theta}{K_h}} \tag{A17}$$

$$E_2^{N} = \frac{L_2^{N}}{L_1^{N}} \frac{1}{z} \frac{1}{\frac{\cos^2 \theta}{K_f} + \frac{\sin^2 \theta + (h/l)}{K_s} + \frac{\cos^2 \theta}{K_h}} \tag{A18}$$

$$K_f = \frac{E_s z t_N^3}{l^3} \tag{A19}$$

$$K_s = \frac{E_s z t_N}{l} \tag{A20}$$

$$G_s = \frac{E_s}{2(1 + \nu_s)} \tag{A21}$$

$$K_h = \frac{G_s z t_N}{l} \tag{A22}$$

where geometric variables are schematically depicted in Figure 9. K_f, K_s, and K_h represent the stiffness values that are defining flexure, stretching, and hinging mechanisms, respectively, G_s is the shear modulus and ν_s is the Poisson's ratio of the parent material. z is unit pattern thickness.

Supporting Information

Supporting Information is available from the Wiley Online Library or from the author.

Acknowledgements

Conflict of Interest

The authors declare no conflict of interest.

Data Availability Statement

The data that support the findings of this study are available in the supplementary material of this article.

Keywords

[1] X. Wu, Y. Su, J. Shi, *Smart Mater. Struct.* **2019**, *28*, 093001.
[2] L.-Y. Zhou, J. Fu, Y. He, *Adv. Funct. Mater.* **2020**, *30*, 2000187.
[3] J.-Y. Lee, J. An, C. K. Chua, *Appl. Mater. Today* **2017**, *7*, 120.
[4] S. M. Montgomery, X. Kuang, C. D. Armstrong, H. J. Qi, *Curr. Opin. Solid State Mater. Sci.* **2020**, *24*, 100869.
[5] G. Stano, G. Percoco, *Extreme Mech. Lett.* **2021**, *42*, 101079.
[6] R. S. Kshetrimayum, *IEEE Potentials* **2005**, *23*, 44.
[7] K. Bertoldi, V. Vitelli, J. Christensen, M. van Hecke, *Nat Rev Mater* **2017**, *2*, 17066.
[8] *Metamaterials* (Eds: T. J. Cui, D. Smith, R. Liu), Springer US, Boston, MA **2010**.
[9] Koryo Miura, *ISAS* **1985**, *618*, 1.
[10] F. Hu, T. Li, *Actuators* **2021**, *10*, 67.
[11] M. Isobe, K. Okumura, *Sci Rep* **2016**, *6*, 24758.
[12] Y.-C. Cheng, H.-C. Lu, X. Lee, H. Zeng, A. Priimagi, *Adv. Mater.* **2020**, *32*, 1906233.
[13] L. J. Gibson, M. F. Ashby, G. S. Schajer, C. I. Robertson, in *Proc. Roy. Soc. Lond. A. Math. Phys. Sci.* **1982**, *382*, 25.
[14] R. Gatt, D. Attard, P.-S. Farrugia, K. M. Azzopardi, L. Mizzi, J.-P. Brincat, J. N. Grima, *Phys. Status Solidi B* **2013**, *250*, 2012.
[15] X. Yu, J. Zhou, H. Liang, Z. Jiang, L. Wu, *Prog. Mater. Sci.* **2018**, *94*, 114.
[16] X. Ren, R. Das, P. Tran, T. D. Ngo, Y. M. Xie, *Smart Mater. Struct.* **2018**, *27*, 023001.
[17] K. E. Evans, M. A. Nkansah, I. J. Hutchinson, S. C. Rogers, *Nature* **1991**, *353*, 124.
[18] K. K. Saxena, R. Das, E. P. Calius, *Adv. Eng. Mater.* **2016**, *18*, 1847.
[19] R. S. Lakes, *Annu. Rev. Mater. Res.* **2017**, *47*, 63.
[20] T.-C. Lim, *Phys. Status Solidi RRL* **2017**, *11*, 1600440.
[21] J. N. Grima, R. Caruana-Gauci, *Nat. Mater* **2012**, *11*, 565.
[22] R. Gatt, J. N. Grima, *Phys. Status Solidi RRL* **2008**, *2*, 236.
[23] Z. G. Nicolaou, A. E. Motter, *Nat. Mater* **2012**, *11*, 608.
[24] R. S. Lakes, T. Lee, A. Bersie, Y. C. Wang, *Nature* **2001**, *410*, 565.
[25] J. Liu, T. Gu, S. Shan, S. H. Kang, J. C. Weaver, K. Bertoldi, *Adv. Mater.* **2016**, *28*, 6619.
[26] H. Zhang, X. Guo, J. Wu, D. Fang, Y. Zhang, *Sci. Adv.* **2018**, *4*, eaar8535.
[27] B. Florijn, C. Coulais, M. van Hecke, *Phys. Rev. Lett.* **2014**, *113*, 175503.
[28] A. Rafsanjani, A. Akbarzadeh, D. Pasini, *Adv. Mater.* **2015**, *27*, 5931.
[29] T. Li, X. Hu, Y. Chen, L. Wang, *Sci. Rep.* **2017**, *7*, 8949.
[30] L. H. Dudte, E. Vouga, T. Tachi, L. Mahadevan, *Nat. Mater.* **2016**, *15*, 583.
[31] G. P. T. Choi, L. H. Dudte, L. Mahadevan, *Nat. Mater.* **2019**, *18*, 999.
[32] F. Pan, Y. Li, Z. Li, J. Yang, B. Liu, Y. Chen, *Adv. Mater.* **2019**, *31*, 1900548.
[33] M. Shirzad, A. Zolfagharian, A. Matbouei, M. Bodaghi, *J. Mech. Behav. Biomed. Mater.* **2021**, *120*, 104594.
[34] H. Rahman, E. Yarali, A. Zolfagharian, A. Serjouei, M. Bodaghi, *Materials* **2021**, *14*, 1366.
[35] F. Wenz, I. Schmidt, A. Leichner, T. Lichti, S. Baumann, H. Andrae, C. Eberl, *Adv. Mater.* **2021**, *33*, 2008617.
[36] A. Sedal, M. Fisher, J. Bishop-Moser, A. Wineman, S. Kota, in *IEEE/RSJ Int. Conf. on Intelligent Robots and Systems (IROS)*, IEEE, Piscataway, NJ **2018**, p. 471.

**ADVANCED
SCIENCE NEWS**

www.advancedsciencenews.com

**ADVANCED
ENGINEERING
MATERIALS**

www.aem-journal.com

[37] H. Jiang, Z. Zhang, Y. Chen, *Appl. Phys. Lett.* **2020**, *117*, 011906.

[38] I. G. Masters, K. E. Evans, *Compos. Struct.* **1996**, *35*, 403.

[39] Y. Prawoto, *Comput. Mater. Sci.* **2012**, *58*, 140.

[40] K. Bertoldi, P. M. Reis, S. Willshaw, T. Mullin, *Adv. Mater.* **2010**, *22*, 361.

[41] Z. Wang, C. Luan, G. Liao, J. Liu, X. Yao, J. Fu, *Adv. Eng. Mater.* **2020**, *22*, 2000312.

[42] H. Yasuda, J. Yang, *Phys. Rev. Lett.* **2015**, *114*, 185502.

[43] Y. Tang, J. Yin, *Extreme Mech. Lett.* **2017**, *12*, 77.

[44] M. J. Mirzaali, S. Janbaz, M. Strano, L. Vergani, A. A. Zadpoor, *Sci. Rep.* **2018**, *8*, 965.

[45] K. R. Olympio, F. Gandhi, *J. Intell. Mater. Syst. Struct.* **2010**, *21*, 1737.

[46] D. T. Farrell, C. McGinn, G. J. Bennett, *Compos. Struct.* **2020**, *238*, 111901.

[47] W. Wu, D. Qi, H. Liao, G. Qian, L. Geng, Y. Niu, J. Liang, *Sci. Rep.* **2018**, *8*, 12575.

[48] R. Gatt, J. P. Brincat, K. M. Azzopardi, L. Mizzi, J. N. Grima, *Adv. Eng. Mater.* **2015**, *17*, 189.

[49] Ultimaker TPU 95A TDS, https://support.ultimaker.com/hc/en-us/articles/360012664440-Ultimaker-TPU-95A-TDS (accessed: January 2022).

[50] J. N. Grima, D. Attard, B. Ellul, R. Gatt, *Cell. Polym.* **2011**, *30*, 287.

[51] A. Kandhari, Y. Wang, H. J. Chiel, R. D. Quinn, K. A. Daltorio, *Soft Robot.*. **2021**, *8*, 485.

[52] A. D. Horchler, A. Kandhari, K. A. Daltorio, K. C. Moses, J. C. Ryan, K. A. Stultz, E. N. Kanu, K. B. Andersen, J. A. Kershaw, R. J. Bachmann, H. J. Chiel, R. D. Quinn, *Soft Robot.* **2015**, *2*, 135.

[53] A. G. Mark, S. Palagi, T. Qiu, P. Fischer, in *IEEE Int. Conf. on Robotics and Automation (ICRA)*, IEEE, Piscataway, NJ **2016**, p. 4956.

[54] M. Liu, Z. Xu, J. J. Ong, J. Zhu, W. F. Lu, in *IEEE/RSJ Int. Conf. on Intelligent Robots and Systems (IROS)*, IEEE, Piscataway, NJ **2020**, p. 7845.

[55] A. Rafsanjani, Y. Zhang, B. Liu, S. M. Rubinstein, K. Bertoldi, *Sci. Robot.* **2018**, *3*, eaar7555.

[56] A. Rafsanjani, L. Jin, B. Deng, K. Bertoldi, *Proc. Natl. Acad. Sci. U.S.A.* **2019**, *116*, 8200.

[57] K. A. Daltorio, A. S. Boxerbaum, A. D. Horchler, K. M. Shaw, H. J. Chiel, R. D. Quinn, *Bioinspir. Biomim.* **2013**, *8*, 035003.

[58] Q. Pan, S. Chen, F. Chen, X. Zhu, *Sci. China Technol. Sci.* **2020**, *63*, 2518.

[59] A. Hasse, K. Mauser, *Soft Robot.* **2020**, *7*, 155.

[60] I. Shufrin, E. Pasternak, A. V. Dyskin, *Int. J. Eng. Sci.* **2015**, *89*, 100.

[61] M. Jiang, N. Gravish, *Smart Mater. Struct.* **2021**, *30*, 035005.

[62] H. Li, Y. Ma, W. Wen, W. Wu, H. Lei, D. Fang, *J. Appl. Mech.* **2017**, *84*, 081006.